Flow Velocity Profiles and Shear Banding Onset in a Semidilute Wormlike Micellar System under Couette Flow

Jorge Delgado,[†] **Hartmut Kriegs,**[‡] **and Rolando Castillo*,**[†]

Instituto de Física, Universidad Nacional Autónoma de México, P.O. Box 20-264, Mexico, D. F., 01000, and Institute für Festkörper Forschung (IFF), Weiche Materie, Forschungszentrum Jülich, D-52425 Julich, Germany

Velocity profiles in Couette flow are measured in a wormlike micellar solution made of cetyltrimethylammonium bromide (CTAB), sodium salicylate (NaSal), and water, at R (= [NaSal]/[CTAB]) = 2 and at R = 4; [CTAB] = 100 mM. Velocity profiles were obtained by using a two-incident beam laser Doppler technique. Profiles reveal that one of the micellar solutions (R = 2) becomes heterogeneous a long time after flow inception, even at very low imposed shear rates. However, profiles do not correspond to what is expected for gradient shear banding, because the fluid splits in one section close to the moving cylinder where the local mean velocity depends linearly on the gap position and in a second section presenting important velocity fluctuations. Close to the static cylinder, there is a third section where the fluid does not flow; it behaves like a slipping block. On the other hand, at high imposed shear rates, the former slipping block flows and presents a linear profile. Here, velocity profiles are consistent with gradient shear banding. The onset of shear banding was observed. The picture of two stable shear bands separated by a thin steady interface is not always valid. Inhomogeneous flow could be observed, although it cannot be classified as shear banding. In addition, conditions can be found where, as shear rate is increased and before shear banding appears, instead of a thin interface, a fluctuating intermediate band can be observed. On the contrary, for the R = 4 solution, the flow never becomes heterogeneous even at high shear rates. Flow curves were measured in a Couette cell under shear rate control in two cases, when stress is sensed with the moving cylinder and when it is sensed with the static cylinder of the cell. Differences between the flow curves can be explained by using the velocity profiles for both solutions.

Introduction

Wormlike micelles (WMs) are semiflexible tubular aggregates in aqueous solution usually made of cationic surfactants and of anionic benzyl hydrophobic moieties. In a restricted range of concentrations, most fluids with WMs behave in a good approximation Maxwell-like, that is, with a single relaxation time in the linear viscoelastic regime. The stress relaxation function can be approximated by $G(t) = G_0 \exp(-t/\tau)$; G_0 (1−1000 Pa) denotes the elastic modulus and τ (1 ms−1000 s) is the relaxation time.[1] The reptation-reaction model[2] for WMs proposes that the relaxation time is the geometric mean of two characteristic times: the time for micellar breaking and recombination and the time for micellar reptation. When WM fluids are submitted to a steady flow, they can show shear banding[1,3] that is a transition between a homogeneous and a nonhomogeneous state of flow[4,5] where macroscopic bands bearing different shear rate coexist in the fluid. In most of the cases, shear bands develop in the velocity gradient direction (gradient banding), although vorticity bands have also been observed (vorticity banding).[6] Gradient banding is usually related with a plateau in the shear stress (σ) versus shear rate ($\dot{\gamma}$) flow curve. Sometimes, shear thickening precedes shear banding; that is, a σ-jump at specific $\dot{\gamma}$ is observed.[7] Commonly, the stress plateau is not completely flat but slopes upward slightly with increasing $\dot{\gamma}$;[5,8,9] this slope could be related to concentration coupling.[8] In a gradient-banding simple scenario, the fluid is divided into two macroscopic regions separated by a thin steady interface of finite width (typically of a few tenths of micrometers). One region flows at high shear rate, showing a strong birefringence[4,5] related to some kind of micellar orientational order. Neutron scattering and nuclear magnetic resonance under shear have confirmed a nematic signature of this region in a particular case.[4] The second region, made mainly of isotropic fluid, flows at low shear rate.[4,5] Micellar aggregates under flow remain cylindrical, and it is expected that the contour length distribution might depend on imposed flow.[10] The specific features of shear banding and of nonlinear mechanical response depend on surfactant concentration,[4,11,12] electrostatic interaction due to micelle screening,[1] and shear conditions, that is, imposed shear stress or shear rate.[13] Also, the kinetics of banding-structure formation and the spatiotemporal dynamics of the interface between bands in the shear banding flow have been studied, revealing the existence of a destabilization process that is not well understood.[14] Theoretical work casts doubts on the theoretical picture of two stable shear bands separated by a steady interface.[15,16] By studying linear stability of the shear banded planar Couette flow for the Johnson−Segalman fluid, it was shown for the case of no stress diffusion that flow is unstable for long waves for almost all arrangements of the two shear bands.[15] In the case of a weak diffusion, a small stabilizing effect is present, although the basic long-wave instability mechanism is not affected.[15] Two driving forces for the instability were identified: discontinuity of shear rate and of normal stress across the interface.

* Corresponding author. E-mail: rolandoc@fisica.unam.mx.
[†] Universidad Nacional Autónoma de México.
[‡] Forschungszentrum Jülich.

Shear banding is considered to be a mechanical-instability consequence of a multivalued nonmonotonic constitutive curve,[17,18] where the stress increases linearly with increasing $\dot{\gamma}$, passing through a maximum and then through a minimum before increasing again. Two branches of the constitutive curve, one at low and one at high shear rates, are separated by a mechanical instable regime where $d\sigma/d\dot{\gamma} < 0$. Mechanical stability requires separation of the fluid in bands where shear stress is a constant throughout the fluid, and bands show different shear rates. A model for shear banding has been proposed in which the high shear branch of the underlying constitutive curve becomes unstable by a coupling between flow and mesostructure, producing a rich variety of spatiotemporal oscillatory and rheochaotic flows resembling experimental observations in shear banding systems.[19] Shear banding has also been considered as a nonequilibrium phase coexistence between an isotropic and a strongly aligned phase, which has a lower viscosity than the quiescent phase.[7,9,20–22] In some cases, band volumes follow an expression equivalent to the lever rule.[20] Olmsted and Lu[7,21,22] have developed a rigid rod-suspension model that has shown a rich nonequilibrium phase behavior. They point out that phase separation is possible under conditions of both common stress (gradient banding) and common strain rate (vorticity banding).

The complex behavior of WM solutions makes it clear that more advanced techniques are required for accessing the flow field and the mesostructural organization as a function of both space and time in the sheared fluid. Measurements of velocity profiles in a Couette cell for a sheared WM fluid made of cethylpyridinium chloride (CPCl)/sodium salicylate (NaSal) in brine have provided evidence for the simple gradient shear banding scenario according to which the effective viscosity drop in the system is due to nucleation and growth of a highly sheared band in the gap, the thickness of which linearly increases with imposed shear rate, following the lever rule.[23] However, this scenario is far from being general. For example, NMR velocimetry measurements have shown that the shape of these bands is different from those seen by optical birefringence.[24–26] In particular, the highly aligned region is not necessarily a phase of low viscosity, and under conditions of near constant stress, shear bands are sometimes subject to rapid positional fluctuations.[24] Local measurements of the extinction angle in a WM solution made of cetyltrimethylammonium bromide (CTAB)/KBr/water at steady flow have shown that the fluid splits into two homogeneous bands in the gradient direction.[11] These bands are separated by a mixed layer, the width of which can reach half of the gap, where the WM orientation with respect to the flow direction varies continuously. WMs in the layer located close to the moving cylinder are almost fully aligned along the flow direction. A comparison of this banding profile with the predictions of the lever rule showed that orientation bands do not coincide in a simple way with the shear bands.[11] Therefore, the band structure found in ref 11 appears strongly different from the simple scenario. However, the authors did not get a clear picture of the mixed layer; the results appear to them consistent with an interface which can be broad, or thin and fluctuating, or as a third phase.[11] The widespread instability obtained by linear instability analysis,[15,16] as well as from accumulating evidence of important deviations from the simple scenario and of important fluctuations in shear banding systems,[11,14,27] suggests that the existing picture of two stable shear bands separated by a thin steady interface needs further research.

Viscoelastic properties of WM solutions of CTAB in water with different proportions of NaSal were studied by Shikata et al.[28,29] At low shear rates, this system follows both a Newtonian behavior[28,29] and the stress-optic law.[30] When increasing the shear rate, a gradient shear banding and a stress plateau are observed,[31,32] even without added salt.[4] At the plateau, the larger imposed shear rate the larger the amount of highly birefringent fluid.[4] When shear banding is reached, velocity profiles have confirmed the existence of two bands with different shear rates in the semidilute regime (NaSal/CTAB: 100/50 mM @ 23 °C).[32] Shear thickening and temporal oscillations in shear stress at the right end of the stress plateau have been observed.[31,32] Shear banding under transient flow[33] and microrheology have also been studied in this system.[34] As we will show in this study, the simple scenario is not valid even in this wormlike micellar system, if surfactant concentrations and R value are modified. Inhomogeneous flow could be observed, although it cannot be classified as shear banding. In addition, as shear rate increases and before shear banding appears, instead of a thin interface, a fluctuating intermediate band can be observed. In this paper, to understand the nature of this peculiar inhomogeneous flow, velocity profiles under Couette flow were determined for two micellar solutions, at $R = 2$ and $R = 4$ ([CTAB] = 100 mM and $T = 20$ °C), by using a two-incident beam laser Doppler technique.[35,36] At both ratios, the system is in the semidilute regime but close to the concentrated regime (mesh size is of the order of persistence length),[34] and micelles are not electrostatically screened by addition of a salt. An important difference between both micellar solutions is the contour length; the contour length of micelles at $R = 2$ is about three times larger than the contour length of micelles at $R = 4$.[34] As we will show, at both ratios, the system presents a similar Maxwellian dynamic viscoelastic spectrum. Consistent with contour lengths, the relaxation time for $R = 2$ is larger than the relaxation time for $R = 4$. Velocity profiles reveal that one of the micellar solutions ($R = 2$) becomes heterogeneous a long time after flow inception, even at very low imposed shear rates. These profiles do not correspond to what is expected for gradient shear banding, because the fluid splits in several regions: one region close to the moving cylinder where local mean velocity depends linearly on gap position, another region with important velocity fluctuations, and, finally, close to the static cylinder, an additional region where the fluid does not flow but behaves like a slipping block. However, at high imposed shear rates, the previous slipping block flows, presenting a linear profile. In the high shear rate regime, velocity profiles are consistent with gradient shear banding. Apparently, we have observed the onset of shear banding. On the contrary, for the $R = 4$ solution, the flow never becomes heterogeneous even at high shear rates. Depending on the kind of instrument used to make the rheometric measurements under Couette flow, strain can be applied by one cylinder, and under shear rate control, the stress can be sensed by the same cylinder or by the other one. We observed important differences between the flow curves obtained with these two methods for the $R = 2$ solution but not for the case of $R = 4$. Others have observed this kind of behavior.[30,31,37] As we will show, velocity profiles can be used to explain the qualitative differences between flow curves for both R values. Finally, we are able to evaluate the utility of the Doppler technique used here to study this kind of systems.

Experimental Section

Materials. CTAB (≥99%) from Fluka (Switzerland) and NaSal (99.5%) from Sigma-Aldrich (MO) were used without further purification. Water was ultrapure Milli-Q water. We used [CTAB] = 0.1 M and two different R values, $R = 2$ and $R =$

Velocity Profiles and Shear Banding Onset

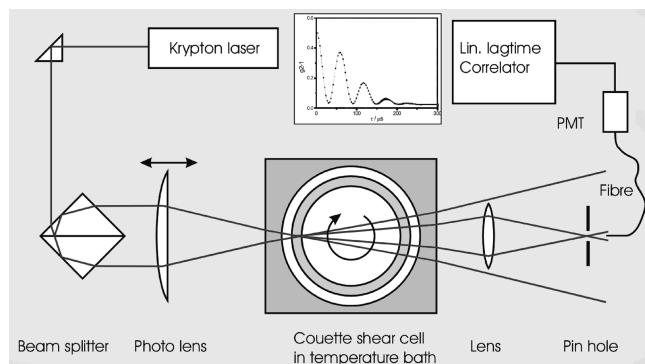*J. Phys. Chem. B, Vol. 113, No. 47, 2009* **15487**

Figure 1. Scheme of the instrument used for measuring the velocity profiles by using a two incident beam laser Doppler technique. The beam intersection length in the radial direction is ~100 μm.

4. One day after preparation, the micellar solutions were centrifuged to remove air bubbles, and then, they were allowed to relax for at least two days. Kraft temperature for these systems have been estimated to be below 20 ^{0}C.[37]

Rheometric Measurements. They were carried out in Couette cells at 20 °C by using two different rheometers. One was an ARES (Rheometric Scientific Inc., NJ), where two different Couette cells were used (diameter of inner cylinder/diameter of outer cylinder: 32/34 mm and 16.5/17 mm). This rheometer works under shear rate control applied on the external cylinder (rotor), and at the same time, shear stress is sensed by using the internal one (stator) with the aid of a torque transducer. The other rheometer was a Bohlin Gemini HRnano (Malvern, U. K.). Here, two different cylinder diameters were used (diameter of inner cylinder/diameter of outer cylinder: 14/15.4 mm and 8/8.8 mm). The software of this rheometer allows us to control the shear rate with the internal cylinder and to sense at the same time the shear stress by using the same internal cylinder (rotor). This rheometer was also used to obtain the dynamic viscolestic spectra of the solutions by using a cone–plate cell (4°, diameter 40 mm) with a strain amplitude of 0.1.

Two different rheological measurements were done: (a) Shear inception experiments. A constant shear rate was imposed on a fluid at equilibrium, and the shear stress response was measured as a function of time. (b) Thixotropic loops (TLs). In a TL, the shear rate is first ramped up (up-shear curve) to some maximum value $\dot{\gamma}_M$, and then, it is ramped down (down-shear curve) at the same rate back to zero. If a fluid was used several times, we allowed the fluid to relax before restarting a new measurement. We consider the fluid completely relaxed when its dynamic viscoelastic spectrum coincides with that of the fluid prior to shearing.

Velocity Profiles. Flow-velocity profiles, $V(r)$, are obtained by measuring the local mean velocity along the gap by using a two-incident beam laser Doppler technique[35,36] in a homemade glass Couette cells, coupled to a motor for controlling the rotational speed of the internal cylinder (Figure 1). These cells have a 2 mm gap width but different cylinder diameters (43/47 mm and 44/48 mm). To control the temperature in the Couette cells, an optical match fluid was used. In our optical setup, a laser beam from a Kr laser ($\lambda = 647$ nm, $I \sim 100$ mW; Spectra Physics, CA) is split in two equal intensity beams, which intersect in a small volume in the gap of the Couette cell filled with the fluid by using a lens (intersection length in the radial direction ~100 μm). Moving this lens allows us to change the position of the beam intersection to measure the local mean velocity of the fluid and to perform scanning cycles along the

Couette cell gap. Scattered light collected by an optical fiber is detected with a photomultiplier tube, and electrical signals are preamplified and shaped with a preamplifier/discriminator (ALV, Germany). Counts per second and correlation functions are obtained with an ALV-Fastcorr correlator with fixed sample times between 75 ns and 400 μs (ALV, Germany). A homemade software correlator was used for longer times. The local mean velocity at the beam intersection is obtained by fitting the experimental intensity correlation function to a decaying cosine function, which depends on the delay time, the local mean velocity, and the scattering vector. In these laser Doppler experiments, the internal cylinder was the rotor, and the external one was the stator (similar to the Bohlin rheometer). For each point, a light scattering measurement lasted between 2 and 5 s to obtain a correlation function, depending on the imposed shear rate and on the gap position. A whole velocity profile along the entire gap was obtained in ~2–4 min.

As mentioned, moving the lens in our instrument allows us to change the position of the beam intersection along the gap. This can be done in steps smaller than 50 times the refractive index (in micrometers). However, to obtain independent (un-correlated) experimental points, we took into account just one measurement of the local velocity for steps that are larger than 100 μm (~120 μm) to make our calculations of local shear rates, because 100 μm is the size of the spatial window defined by the beam intersection. Velocity-versus-gap-position diagrams presented with a step less than 100 μm, typically 60–80 μm, are intended to present a general shape and the main features of the flow.

Birefringence and Light Attenuation. Birefringence and light attenuation under flow were measured by using the same homemade glass Couette cells as the ones described above. Birefringence is obtained from the phase-shift coefficients in the principal directions,[36] and light attenuation is obtained from the different absorption coefficients in the same principal directions as follows:[36,38,39] A linear polarized beam is sent to a rotating half-wave retardation platelet, to get a linear polarized light beam rotating with a frequency 2ω. This beam is sent to the Couette cell crossing the gap, filled with the fluid, twice along the velocity gradient direction. It is assumed that for each principal optical axis, the birefringence phase shift φ_j and the light attenuation τ_j are described by terms of the form $\exp(i\varphi_j) \exp(-(1/2)\tau_j)$,[39] where j refers to the corresponding optical axis. After the beam has crossed the gap twice, it is split in two equally intense beams. One of these beams is sent into a detector where light attenuation is obtained by using the following expression:[39]

$$I = \frac{I_0}{2} e^{-1/2(\tau_x+\tau_y)} \cosh \delta''$$
$$(1 - \tanh \delta'' \cos 2\alpha \cos 4\omega t - \tanh \delta'' \sin 2\alpha \sin 4\omega t)$$

Where, I_0 is the intensity of the light coming into the gap, $\delta'' = (1)/(2)(\tau_x - \tau_y)$ is the light attenuation, and α is the angle between the original coordinate system and the direction of the principle axes. The second beam is sent to a quarter lambda platelet and is analyzed with a Glan-Thompson polarizer. Afterward intensity is measured according to the expression:[39]

$$I = \frac{I_0}{4} e^{1/2(\tau_x + \tau_y)} \cosh(\delta'') \left\{ 1 - \left([\tanh(\delta'') \cos(2\alpha) + \frac{\sin(\varphi_x - \varphi_y)}{\cosh(\delta'')} \sin(2\alpha)] \cos(4\omega t) - \left([\tanh(\delta'') \sin(2\alpha) - \frac{\sin(\varphi_x - \varphi_y)}{\cosh(\delta'')} \cos(2\alpha)] \sin(4\omega t) \right) \right\}$$

The coefficients of the 4ω frequency components are measured and filtered out by using two lock-in amplifiers. $\varphi_x - \varphi_y$ is the birefringence.

Results and Discussion

a. Velocity Profiles for $R = 2$ and $R = 4$. An imposed shear rate, $\dot{\gamma}_{imp}$, was applied to the WM fluid at rest by means of the inner moving cylinder (step-strain rate), and the fluid velocity profile was obtained, usually a long time after the inception of flow. Along the paper, the imposed shear rate is used as the nominal value imposed by the rheometer (angular velocity of the moving cylinder times the average cell radius over the gap length); it is not considered as the actual shear rate in the fluid. In contrast, local shear rates, $\dot{\gamma}_L$, are reported; they come from the slope of the linear fitting of $V(r)$ versus r. These values have the advantage that they are independent of slip at boundaries. For $R = 2$, the main signature of velocity profiles is that the flow becomes heterogeneous even at very low imposed shear rates, where profiles present two or more sections, corresponding to regions in the fluid that have a different local shear rates ($\dot{\gamma}_L$) in an apparent stationary flow. However, there are important velocity fluctuations at some positions in the gap. At high imposed shear rates, the profiles become consistent with those of shear banding. In contrast, for $R = 4$, the flow is always homogeneous.

Velocity Profiles for $R = 2$. *Velocity Profiles for $\dot{\gamma}_{imp} < 0.20$ s^{-1}.* Figure 2a presents typical velocity profiles for $\dot{\gamma}_{imp} < 0.20$ s^{-1} obtained by using the 44/48 cell. The flow velocity profiles present two different regions, one close to the inner moving cylinder (gap position $X_G = 2$ mm), where $V(r)$ depends almost linearly on the position, and another region close to the outer static cylinder (gap position $X_G = 0$). In the latter region, $V(r)$ is almost constant; that is, the material is moving as a slipping block, which is slipping on the static boundary with a size of $\sim$0.6 mm, although it could be thinner. $V(r)$ just close to the moving cylinder roughly coincides with the cylinder velocity; however, velocity fluctuations here are significant and attributable to some slip on the moving boundary that is of the order of 10% of the local mean velocity. In this technique, Doppler frequency is determined by fitting to a decaying model function, and it disperses around the real value. As long as the model function does not describe the data, systematic shifts of the frequency in either direction are possible. For this technique, the uncertainty of the fitting with good correlation functions using spherical latex particles is below 5%. Between 0.9 and 1.2 mm, $V(r)$ presents slope changes. The only curve ($\dot{\gamma}_{imp} = 0.01$ s^{-1}) that has a constant slope along the gap and with a negligible slipping is the lowest one corresponding to an actual $\dot{\gamma} = 0.01 s^{-1}$. These velocity profiles do not correspond to the simple scenario of shear banding, because the fluid does not split into two regions of constant shear rate, because one region of the fluid does not flow. Figure 2b shows a sequence of velocity profiles as a function of elapsed time after flow inception for the 43/47 cell at $\dot{\gamma}_{imp} = 0.1$ s^{-1}. In addition, we included in this figure the average of the local mean velocity (for a period of $\sim$12 min) for specific positions in the gap. In
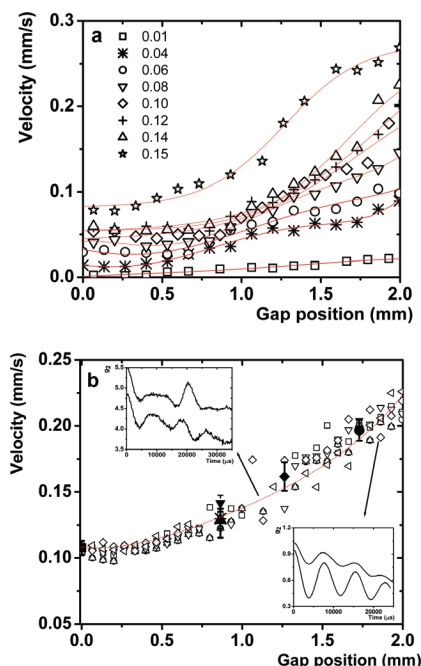

Figure 2. Velocity profiles under Couette flow (2 mm gap, $R = 2$). (a) Velocity profiles under stationary flow for the 44/48 cell determined for independent points. Measurements every $\sim$120 μm. The moving boundary is at $X_G = 2.0$ mm, and the static boundary is at $X_G = 0$. Legend shows the imposed shear rate in s^{-1}. Lines are guides to the eye. (b) Velocity profiles determined as time elapses for the 43/47 cell, at 13 ($\square$), 63 ($\bigcirc$), 165 ($\triangledown$), 237 ($\diamond$), and 320 (open tilted left triangle) min after flow inception ($\dot{\gamma}_{imp} = 0.10$ s^{-1}). Measurement every $\sim$60 μm. Line is a guide to the eye for the 320 min curve. Full symbols show the time average for the local mean velocity during 12 min. Insets: Examples where a local mean velocity can be determined from the intensity correlation function (bottom) and where a local mean velocity cannot be evaluated (top).

most of the positions, correlation functions are clearly defined, as can be observed in the lower inset of Figure 2b. There is a thin intermediate region located at $X_G \approx 1.1$ mm, where local mean velocity fluctuates even at a long time after flow inception. $V(r)$ usually cannot be determined there, because correlation functions are not exponentially modulated single-cosine functions (upper inset in Figure 2b). For this reason, points are missing in this intermediate region in Figure 2b. This thin region is similar to those in a polymer melt fracture occurring when a large-amplitude oscillatory shear is applied on entangled polymer solutions.[40,41] A model was developed by de Gennes[42] for slippage planes in entangled polymers based on a balance between reptation bridging and shear debonding. In this model, the formation of a slip plane could occur, but because the entangled state is locally stable, some external agent (solid surface or dust particles) has to nucleate that slip plane. Once this plane is initiated, it will stay. For WMs solutions, if micellar breaking were proposed as the nucleating mechanism for the slip plane formation and if the inverse of the breaking micellar time were used to estimate $\dot{\gamma}_{imp}$, the shear rate would be too large. Therefore, this proposed model cannot be directly used to explain our observations as a melt fracture.

Local shear rates, $\dot{\gamma}_L$, for the linear region close to the moving cylinder (of a size $\sim$1 mm) are presented as a function of $\dot{\gamma}_{imp}$ in Figure 3a. $\dot{\gamma}_L$ was computed from the slope of velocity profiles determined from independent experimental points. Here, the relation between $\dot{\gamma}_L$ and $\dot{\gamma}_{imp}$ is linear no matter the size of the Couette cell. The slopes are 0.81 and 0.92 for the 43/47 and 44/48 cells, respectively. Slopes were obtained by linear fitting
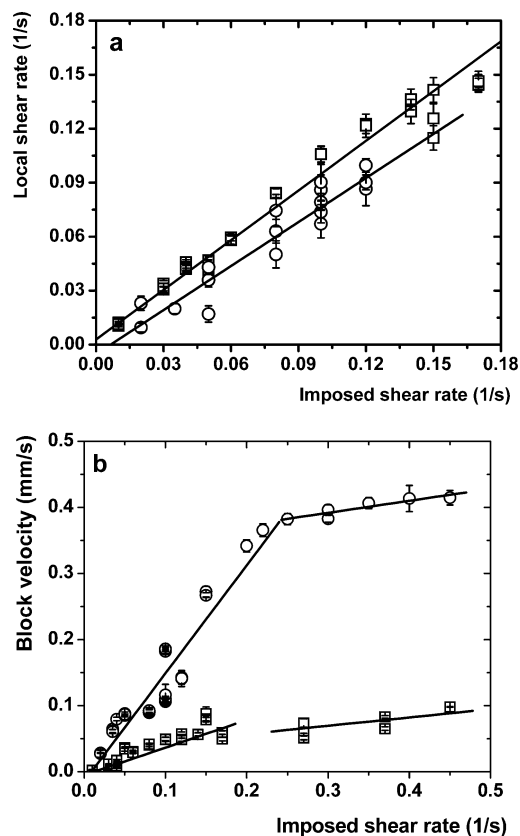
Velocity Profiles and Shear Banding Onset

J. Phys. Chem. B, Vol. 113, No. 47, 2009 **15489**

Figure 3. (a) Local shear rate only for the region close to the moving cylinder of a size ~1 mm vs $\dot{\gamma}_{imp}(R = 2)$. Experimental points come from two different Couette cells; 44/48 cell ($\square$) and 43/47 cell ($\bigcirc$). (b) Mean velocity of the slipping block next to the static cylinder. Symbols for different cells are the same as those used in panel a. Continuous lines correspond to linear fittings as described in the text.

(correlation coefficients better than 0.96). Here, we observe that the fluid close to moving boundary presents a local shear rate lower than the imposed one: ~20% for the 43/47 cell and ~10% less for the 44/48 cell. Velocity fluctuations are apparently due to slipping on the moving wall, as is better illustrated in Figure 2b (dispersion of velocity at $X_G = 2$). In Figure 3b, we present the local mean velocity for the slipping block near the static cylinder for both Couette cells. The slipping velocity of the block, v_b, increases linearly with the imposed shear rate; that is, $v_b = k\dot{\gamma}_{imp}$, where the constant k depends on the size of the cell. These constants are 0.46 and 1.61 mm for the 44/48 and 43/47 cells, respectively. Constants were obtained with linear fitting (correlation coefficients are better than 0.91). As we can observe, velocity fluctuations of the slipping block close to the wall are not as important as those for the fluid close to the moving wall (Figure 2b, velocity dispersion at $X_G = 2$).

Velocity profiles for 0.20 s^{-1} < $\dot{\gamma}_{imp}$ < 0.45 s^{-1}. In Figure 4, we present typical velocity profiles in the range of $0.20 < \dot{\gamma}_{imp}$ < 0.45 s^{-1}, measured a long time after flow inception in the 44/48 cell. For comparison, in one case, five profiles are presented ($\dot{\gamma}_{imp} = 0.27$ s^{-1}). In this range of $\dot{\gamma}_{imp}$, velocity fluctuations are larger than in the case when $\dot{\gamma}_{imp} < 0.2$ s^{-1} and more extended along the gap. Velocity fluctuations lead to bad correlation functions in our technique. The average velocity should remain constant in the measurement volume as long as the time correlation functions is averaged. When the average time and the measurement volume cannot be chosen small enough, contributions of many different Doppler frequencies destroy the oscillating correlation function. As an example, in three of the profiles for $\dot{\gamma}_{imp} = 0.27$ s^{-1}, we have included thick

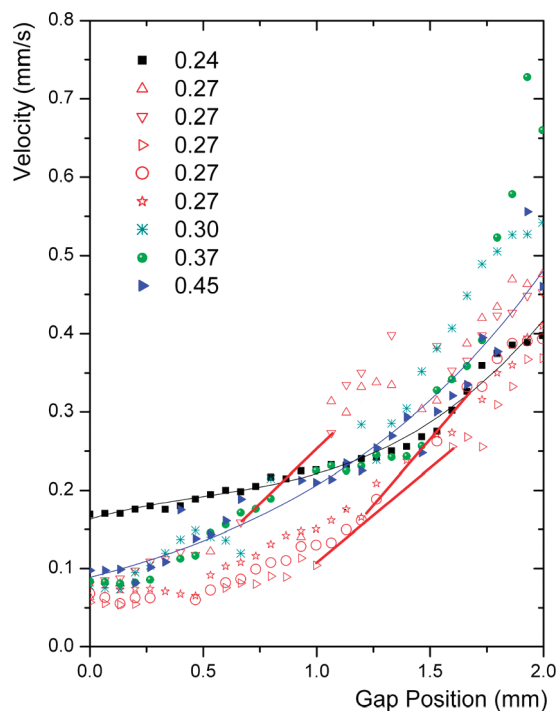**Figure 4.** Typical velocity profiles for $R = 2$ in the range 0.20 s^{-1} < $\dot{\gamma}_{imp} \leq 0.45$ s^{-1} (measurement every ~60 μm) for the 44/48 cell. Thin (black and blue) lines are guides to the eye. For three profiles of all the cases presented for $\dot{\gamma}_{imp} = 0.27$ s^{-1}, we have included thick (red) lines to point out the sectors where experimental points are missing because of large fluctuations.

(red) lines, where experimental points are missing because of large fluctuations; the other two profiles for this case also have gaps without experimental points. Notwithstanding the large fluctuations, several features can be observed. Most of the time, three regions can be defined for a velocity profile. A region close to the inner moving cylinder ($X_G = 2$) of approximately 0.5 mm, where $\dot{\gamma}_L$ depends almost linearly on position. The region corresponding to the slipping block found at low $\dot{\gamma}_{imp}$ reduces now to a slim band close to the static cylinder ($X_G = 0$); its velocity increases slightly as $\dot{\gamma}_{imp}$ increases, as presented in Figure 3b for $\dot{\gamma}_{imp} > 0.20$ s^{-1}. Between these regions, there is an intermediate region where the fluid acquires a linear profile, with a slope not necessarily equal to that of the region close to the moving cylinder. This intermediate region is located approximately between $X_G = 0.75$ mm and $X_G = 1.6$ mm, but its position fluctuates (lines in Figure 4). Here, velocity measurements are difficult to obtain because of intense velocity fluctuations. Nevertheless, in some measurements, a less common type of profile appears, where the fluid seems to be formed by just two coexisting regions. They can appear at $\dot{\gamma}_{imp}$ values where, in other experiments three regions were observed. Here, in the region where previously a slipping block was observed, $V(r)$ depends now linearly on the position with a small slope (X_G from 0 to ~1.0 mm for $\dot{\gamma}_{imp} = 0.24$ s^{-1} in Figure 4), and in the coexisting region close to the moving cylinder, $V(r)$ is also a linear function of the position, with a different slope. All seem to indicate that, in this range of $\dot{\gamma}_{imp}$, slipping and fluctuations are playing an important role. The system is trying to reach a state with two bands; this is better observed probably when $\dot{\gamma}_{imp}$ is larger. In Figure 5, we present typical velocity profiles as time elapses after a step strain rate of $\dot{\gamma}_{imp} = 0.27$ s^{-1} imposed on the fluid. To measure V as a function of time, our light scattering instrument scans the whole gap in 226 s. The detector window is opened for measuring for approximately
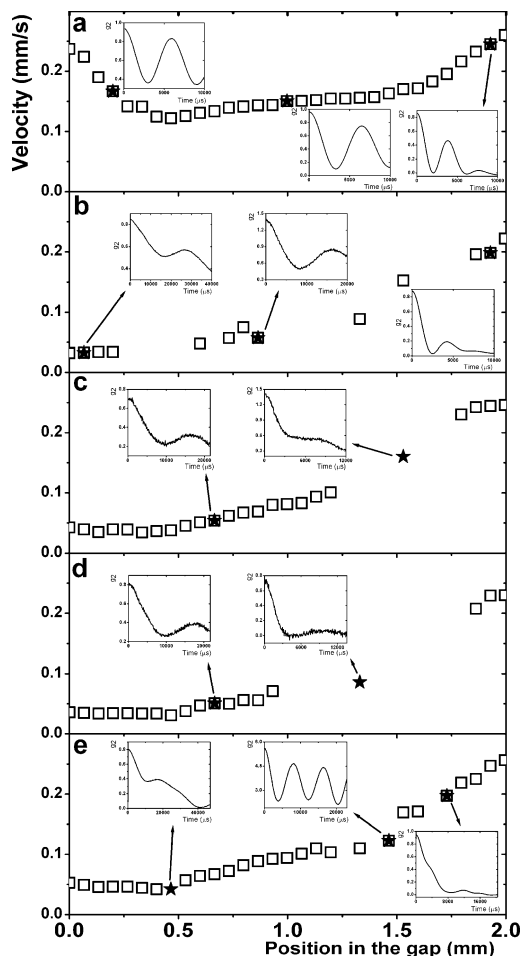
Figure 5. Consecutive velocity profiles obtained for $\dot{\gamma}_{\mathrm{imp}} = 0.27 \ \mathrm{s}^{-1}$ after the inception of the flow ($R = 2$) measured in the 44/48 cell. Velocity profile measured from position $X_{\mathrm{G}} = 0$ (static cylinder) to $X_{\mathrm{G}} = 2$ mm (moving cylinder). Insets in all graphs show correlation functions in positions marked with a star (★). (a) The first velocity profile (at top) was obtained during the first 226 s after inception of the flow. (b) After 226 s, the local mean velocity can be determined near the boundaries. (c) and (d) After 452 s, many points in the gap acquire a stable velocity profile. (e) After ~15 min, a local mean velocity can be computed almost anywhere along the gap. Three regions in the fluid can be observed.

5 s at each position. Several scans were made sequentially after the imposed step strain rate (at $t = 0$). In the first scanning (Figure 5a), $V(r)$ shows three different regions in the fluid. Close to the static cylinder, the slope of the curve is less than zero because of the elastic character of the fluid. Curiously, here, the correlation functions are perfectly defined, in spite of being a transitory response. In the next scanning (Figure 5b), fluid velocities near the cylinders are well determined. In contrast, in the middle of the gap, we are not able to determine $V(r)$ in many positions because of fluctuations. In subsequent scannings, $V(r)$ is determined in most of the positions along the gap (Figure 7c,d), except in a section of the fluid ($X_{\mathrm{G}} \approx 1.25-1.75$ mm) where fluctuations did not allow us to acquire the local mean velocities. Approximately 15 min after flow inception, some regions of the fluid arrive to a stationary state similar to those observed in Figure 4, where $V(r)$ can be measured along the gap, except in some thin bands. Now, apparently three regions can be clearly observed (Figure 5e): a linear region close to the moving cylinder, an intermediate region, and the slipping block. At this $\dot{\gamma}_{\mathrm{imp}}$, slipping on the moving boundary is typically less than 10%. Decruppe et al.[32] have also found velocity profiles
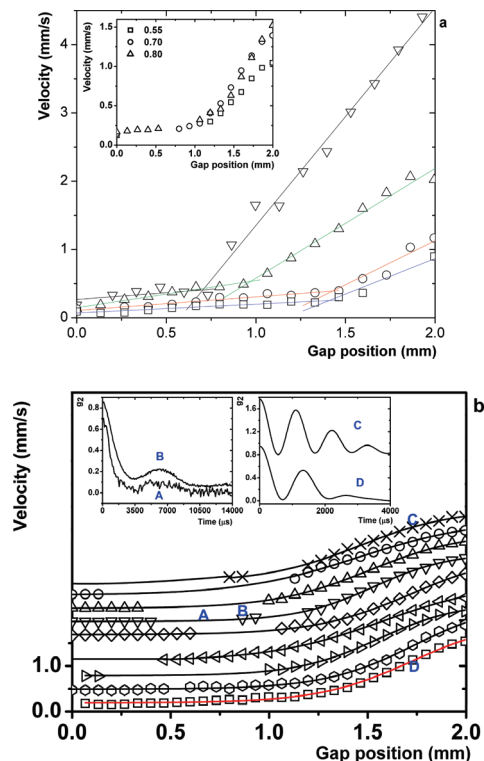

Figure 6. (a) Velocity profiles for $\dot{\gamma}_{imp} \geq 0.45 \ \mathrm{s}^{-1}$ under stationary flow conditions obtained by using the 44/48 Couette cell ($R = 2$), measurement every ~120 μm. $\dot{\gamma}_{imp}(\mathrm{s}^{-1}) = 0.45$ (□), 0.70 (○), 1.00 (△), and 2.00 (▽). Lines are linear fittings. Inset: Velocity profiles determined by using the 43/47 Couette cell. Legend denotes $\dot{\gamma}_{imp}$ in s^{-1}. (b) Several successive velocity profiles (measurement every ~60 μm) at constant $\dot{\gamma}_{imp} = 0.80 \ \mathrm{s}^{-1}$ determined at 4 (top), 25, 40, 60, 90, 257, 272, 331, and 345 (bottom) min after flow inception. All velocity profiles are originally superimposed, but for a better visualization, they were successively displaced upward starting from the curve for 345 min; vertical axis labels correspond to the measured values for this last curve (line in red). Lines are a guide to the eye. Right inset: Correlation functions for the same position ($X_{\mathrm{G}} = 1.7$ mm) at two different times: 4 min (C) and 345 min (D) after flow inception. Left inset: A and B locations where it was possible to observe how fluctuations destroy correlation and local mean velocity cannot be obtained.

with three linear segments at the onset of the stress plateau. A connection between their and our measurement will come later.

Velocity profiles for $\dot{\gamma}_{imp} > 0.45 \ s^{-1}$. In Figure 6, we present velocity profiles for $\dot{\gamma}_{\mathrm{imp}} > 0.45 \ \mathrm{s}^{-1}$, where two regions in the fluid are observed. We restrict our measurements for shear rates below $\dot{\gamma}_{\mathrm{imp}} = 2.5 \ \mathrm{s}^{-1}$, because air bubbles are developed in the solution at higher shear rates. The slipping block that appeared for $\dot{\gamma}_{\mathrm{imp}} \leq 0.45 \ \mathrm{s}^{-1}$ close to $X_{\mathrm{G}} = 0$ has been transformed in a region showing a linear velocity profile with a small slope, where $\dot{\gamma}_{\mathrm{L}}$ depends linearly on $\dot{\gamma}_{\mathrm{imp}}$. The linear region close to the moving cylinder, which is observed at lower $\dot{\gamma}_{\mathrm{imp}}$ values, still stays as a region where the local mean velocity is a linear function of position. On the moving boundary, fluid velocity is 2% lower than tangential cylinder velocity, and on the static boundary, the local mean velocity of the fluid is ~5-10% of the moving wall velocity. In general, at this $\dot{\gamma}_{\mathrm{imp}}$, slipping seems to be playing a minor role. In this figure, apparently there is no intermediate region. The lever rule, $\dot{\gamma}_{imp} = \dot{\gamma}_{\mathrm{L}}\phi_{\mathrm{stator}} + \dot{\gamma}_{\mathrm{H}}\phi_{\mathrm{rotor}}$, is apparently followed; ϕ is volume fraction, and indexes refer to the fluid regions close to the cylinders supporting high (H) and low (L) local shear rates. The shear rate for the involved phases can be estimated from the slope of the straight lines of Figure 6a obtained with linear fitting: $\dot{\gamma}_{\mathrm{L}} = 0.20, 0.40, 0.20,$

Velocity Profiles and Shear Banding Onset

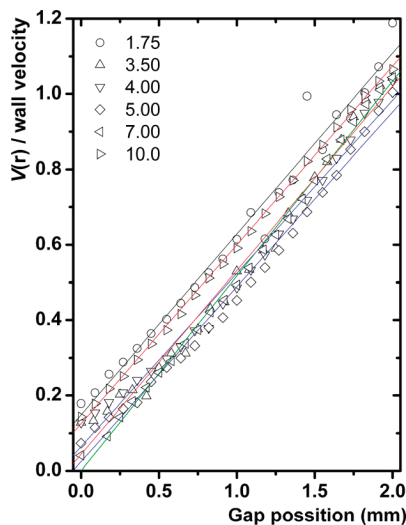*J. Phys. Chem. B, Vol. 113, No. 47, 2009* **15491**

Figure 7. Normalized local mean velocity (local mean velocity divided by the wall velocity) vs gap position for $R = 4$. Local mean velocities were measured every ~80 μm. The legend marks the imposed shear rate in s^{-1}. Lines are guides to the eye made with linear fittings.

and 0.13 s^{-1} for $\dot{\gamma}_{imp} = 2.00$, 1.00, 0.70, and 0.45, respectively, and $\dot{\gamma}_H = 3.19$, 1.60, 1.29, and 1.04 s^{-1} for the same sequence of $\dot{\gamma}_{imp}$, respectively. Averaging these values produces $\dot{\gamma}_L \approx 0.23$ s^{-1} for the phase supporting the lowest shear rate and $\dot{\gamma}_H \approx 1.78$ s^{-1} for the phase supporting the highest shear rate. Calculating $\dot{\gamma}_{imp}$ by using the lever rule with the averaged values and with the ϕ_i coming from the line crossings of Figure 6a gives an error of −38.5, 2.7, −4.1, and 54% from the actual imposed shear rate, respectively. Figure 6b presents successive velocity profiles when $\dot{\gamma}_{imp} = 0.80$ s^{-1} as a function of elapsed time since flow inception. The first velocity profile was determined 4 min after inception of flow. The region of the gap close to the moving cylinder, $X_G = 2$ mm, presents a well-defined $\dot{\gamma}_L$ just few minutes after flow inception. This region remains stable for a long time (~345 min). However, for some positions between $X_G \approx 0-1$ mm, the fluid does not seem to reach easily a steady state even a long time after flow inception because fluctuations last too long (missing points in Figure 6b). The location of the sector where velocity fluctuates changes as time elapses, but in this range, it is always close to the static cylinder. After a long time, the system ends as in Figure 6a. Here, also the fluid approximately follows the lever rule ($\dot{\gamma}_L = 0.19$ s^{-1} and $\dot{\gamma}_H = 1.69$ s^{-1}, % error with respect to $\dot{\gamma}_{imp} = 6\%$). In summary, at high shear rates ($\dot{\gamma}_{imp} \geq 0.45$ s^{-1}), the micellar solution at $R = 2$ reaches a steady state where macroscopic bands coexist supporting different shear rates.

Velocity Profiles for $R = 4$. In Figure 7, velocity profiles for $R = 4$ are presented for several imposed shear rates. Here, we can observe that the local mean velocity is a linear function of position along the gap. For this R, even at relatively high $\dot{\gamma}_{imp}$, we never observed a heterogeneous flow in the Couette cell. Close to the static wall, slipping is observed; in most of the cases, it decreases as $\dot{\gamma}_{imp}$ increases, and it is in the range of 5−15% of the moving wall. Slipping close to the moving wall is negligible.

b. Dynamic Viscoelastic Spectra. Figure 8 shows the dynamic viscoelastic spectra for the micellar solutions of interest here at 20°C. Both fluids are Maxwellian at low frequencies. The elastic moduli are $G_o = 66$ Pa for $R = 2$ and $G_o = 46$ Pa for $R = 4$. Relaxation times are $\tau = 15$ s for $R = 2$ and $\tau = 0.7$ s for $R = 4$. These values are close to previously published data for this system in similar conditions,[31,32] and from them,
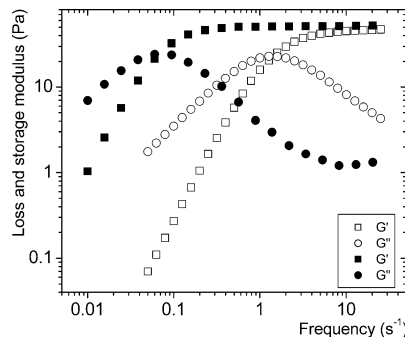

Figure 8. Dynamic viscoelastic spectra for the wormlike micellar system CTAB/NaSal/water at 20 °C for $R = 2$ (full symbols) and for $R = 4$ (open symbols). [CTAB] = 100 mM.
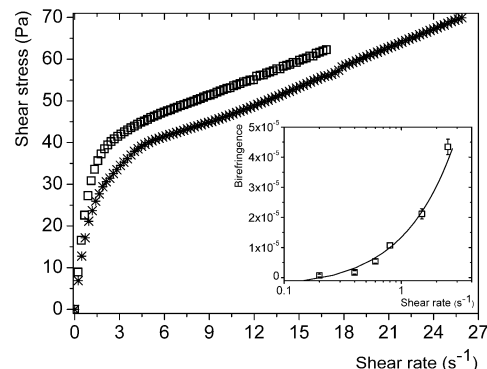

Figure 9. Typical up-shear curves made during TLs for $R = 4$; ramp = 0.0037 s^{-2}. The stress is sensed with different cylinders forming the Couette cell. Stress sensed with the rotor where shear rate is also imposed (□, Bohlin rheometer). Stress sensed with the inner static cylinder (∗, Ares rheometer). Inset: Birefringence under shear rate control as a function of imposed shear rate. Continuous line is a linear fitting.

zero shear viscosity ($G_o\tau$) can be evaluated: 990 Pa s for $R = 2$ and 32.2 Pa s for $R = 4$. According to these experiments and to the results of previous studies,[25,26,31,32] both micelar solutions are made of WMs, and their contour-length sizes are in agreement with the measured relaxation times values for each solution.[34]

c. Shear Flow Curves. Stress response of the fluid is measured by using two different rheometers in Couette flow. Each one imposes the shear strain rate with a different cylinder of their Couette cells, and the inner cylinder in both cells measures the stress response. However, in one case, the inner cylinder is rotating (rotor), and in the other, it is static (stator). Flow curves for $R = 4$ are equivalent. Small differences are the results of different cell curvatures, gap sizes, slipping boundary conditions, and end defects at the bottom of the cell. However, for $R = 2$, curves are different. This difference has been noted previously for this particular fluid. For $R = 2$, Humbert et al.[30] did not observe strain hardening in NaSal/CTAB, when stress was sensed by using the moving cylinder of a Couette cell of a rheometer; meanwhile, Inoue et al.[37] and Assouzi et al.,[31] sensing the stress by using the static cylinder, found strain hardening. There is no clear explanation of why these two different rheological measurements, both under shear rate control, provide different results in WM fluids. As shown below, slipping and shear banding could be of help in explaining the differences between the flow curves.

TLs, Birefringence under Shear for $R = 4$. Figure 9 presents typical stress responses for $R = 4$ during the ramping up for both kinds of stress measuring modes (Bohlin and ARES
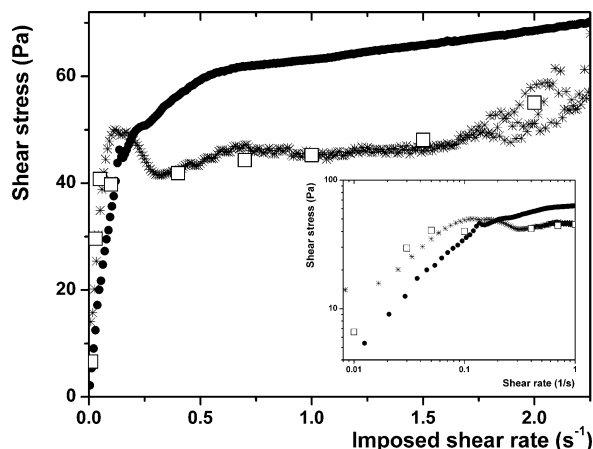
Figure 10. Typical up-shear curves made during TLs ($R = 2$). The stress is sensed with different cylinders forming the Couette cell. Stress sensed with the rotor where strain is also imposed (●, ramp = 0.0012 s^{-2}, Bohlin rheometer). Stress sensed with static cylinder (*, ramp=0.0007 s^{-2}, Ares rheometer). Hollow squares show the mean shear stress coming from shear inception experiments using the static cylinder (Ares rheometer). Inset: same chart but in a log–log plot.

rheometer). In both cases, the imposed shear rate is incremented with a very small ramp to ensure a quasi-stationary state of flow $((\Delta\dot{\gamma})/(\Delta t) = 0.0037$ $s^{-2})$. Flow curves present a Newtonian behavior at $\dot{\gamma}_{imp} < 1$ s^{-1}. As $\dot{\gamma}_{imp}$ increases, the fluid presents shear thinning in the range of 1 $s^{-1} < \dot{\gamma}_{imp} < 5$ s^{-1}. When shear rate reaches $\dot{\gamma}_{imp} \approx 5$ s^{-1}, the onset of a second Newtonian behavior with a lower viscosity is found. Flow-curve upper boundaries are limited by air-bubble formation; this explains the difference in the flow-curve endings. At this low ramping velocity, down-shear curves can be traced over the up-shear curves. Notwithstanding the differences in measuring instruments and in Couette cells, both flow curves actually describe the same physical situation; they present the same shape, and apparent low shear viscosities (26 Pa s for the Ares and 33 Pa s for the Bohlin) agree reasonably well with the zero shear viscosity evaluated from the viscoelastic spectra. In addition, fluid birefringence under shear increases linearly with $\dot{\gamma}_{imp}$ until $\dot{\gamma}_{imp} = 2.5$ s^{-1} (inset Figure 9). In this range, the fluid is thinning, but the velocity profile is linear (Figure 7). Therefore, we infer that a continuous alignment of WMs is under way as $\dot{\gamma}_{imp}$ increases. The flow curve at $R = 4$ recalls those curves above the critical point in a master dynamic phase diagram.[5] The system is above the coexistence dome where phases supporting different shear rates cannot coexist.

In summary, the WM solution at $R = 4$ is a rheo-thinning fluid between two Newtonian regimes. It does not matter what cylinder is used to sense the stress when shear is imposed, because velocity profiles show that this is a homogeneous fluid where local mean velocity depends linearly on position. Although some slipping can be present on the static boundary (Figure 7), nothing suggests shear banding, slipping blocks, or some flow discontinuity.

TLs, Birefringence, and Light Attenuation under Shear for $R = 2$. Figure 10 presents typical stress responses for $R = 2$ in TLs during the ramping up for both kinds of stress measuring systems. Again, the imposed shear rate increment was very slow to ensure a quasi-stationary state of flow. When shear stress is sensed with the inner rotating cylinder, that is, when $\dot{\gamma}$ is also imposed, the flow curve is linear for $\dot{\gamma}_{imp} < 0.1$ s^{-1}. As the shear rate increases, the fluid shear thins in the range of $0.1 < \dot{\gamma}_{imp} < 0.75$ s^{-1}, although the curve where the fluid is thinning is not completely smooth. When shear rate reaches $\dot{\gamma}_{imp} \approx 0.75$ s^{-1}, a

second linear regime is found in the flow curve. For nominally identical samples, this measuring system provides reproducible up-shear curves if ramping is small; that is, $(\Delta\dot{\gamma})/(\Delta t) \leq 0.0040$ s^{-2}. Below this ramping rate, down-shear curves from TLs can be approximately traced over the up-shear curves. This behavior is similar to what it is observed for $R = 4$. In contrast, when stress response is sensed by using the inner static cylinder and $\dot{\gamma}$ is imposed with the external cylinder, the flow curves are not reproducible for nominally identical samples no matter if very slow ramps are used. In this case, up-shear and down-shear curves never coincide. In Figure 10, at $\dot{\gamma}_{imp} \leq 0.1$ s^{-1}, shear stress increases almost linearly with $\dot{\gamma}_{imp}$ (inset Figure 10). For larger $\dot{\gamma}_{imp}$, strain hardening precedes a zone where shear stress fluctuates. Here, the flow behavior can be described as a stress plateau, because despite fluctuations, the shear stress is constant on average. Mean shear stress values from shear inception experiments follow closely the up-shear curve. Stress oscillations at the beginning of this plateau ($\dot{\gamma}_{imp} < 2$ s^{-1}) are of small amplitude. However, for $\dot{\gamma}_{imp} > 2$ s^{-1}, stress oscillations are of large amplitude, and the mean shear stress values also increase. We will come back to these stress oscillations below.

Although, from our birefringence measurements, the contribution to birefringence from every part of the fluid cannot be known, our measurements (not shown) were in agreement with previous reported results.[30] In our results for $0.02 < \dot{\gamma}_{imp} < 0.10$ s^{-1}, birefringence increases linearly with the imposed shear rate; that is, $(\varphi_x - \varphi_y) \approx \sigma$. In this range of $\dot{\gamma}_{imp}$, δ^* is small ($\sim 1.1 \times 10^{-7}$), constant with respect to changes in $\dot{\gamma}_{imp}$, and two orders of magnitude below birefringence values.

Relation between Shear Flow Curves and Velocity Profiles. In spite of using exactly the same techniques and protocols for obtaining velocity profiles and flow curves for the micellar solutions studied here, depending on where stress is sensed, measured flow curves are different for $R = 2$. This must be attributable to heterogeneous flow and to slipping, both starting at very low $\dot{\gamma}_{imp}$ values. For flows where $\dot{\gamma}_{imp} < 0.20$ s^{-1}, we do not observe shear banding in the solution. Although many profiles reveal a heterogeneous flow, $\dot{\gamma}_{imp}$ is not in the stress plateau. It is in the ascending part of the flow curves, where a continuous alignment of WMs is taking place as concluded by birefringence measurements. Here, the flow is partially dominated by slipping as confirmed by the formation of a slipping block. At $\dot{\gamma}_{imp} \leq 0.1$ s^{-1}, $\sigma \approx \dot{\gamma}_{imp}$ (inset Figure 10), and from Figure 3b, the velocity of the slipping block is $v_b = k\dot{\gamma}_{imp}$; as a consequence $\sigma \approx v_b$. This observation is similar for the case of entangled polymers under slip on a flat surface, where $\sigma \approx k_0 v_b$.[43] Here, v_b is the slip velocity, and k_0 is a constant. At higher flows, where $0.20 < \dot{\gamma}_{imp} < 0.45$ s^{-1}, the fluid, as it is sensed by the stator, is under strain hardening; shear stress fluctuates, and the fluid is in heterogeneous flow as reveled by velocity profiles. There are velocity fluctuations at sectors not always in the same position. The fluid seems to be at an instability trying to determine what the more stable state is. For the case of flow curves where stress is sensed with the rotor, the fluid is under shear thinning. For the same system studied here, Decruppe et al.[32] have found three linear segments in the velocity profiles at the onset of the plateau. They pointed out that this peculiar behavior could be an artifact of their particular experimental device. We have reproduced results similar to those of these authors, that is, three regions in the fluid at the onset of the plateau, but by employing a different technique; threfore, we think that this result is robust. Finally, at $\dot{\gamma}_{imp} > 0.45$ s^{-1}, the solution splits into two linear regions. Here, the imposed shear rates correspond to those at the plateau in the flow shear curves,

Velocity Profiles and Shear Banding Onset

J. Phys. Chem. B, Vol. 113, No. 47, 2009 **15493**

as the static cylinder senses it. Here, the fluid apparently follows the lever rule. For the flow shear curves sensed with the rotor, the system is in the second linear regime. The origin of different flow curves depends on, in either case, whether the transducer is on the rotor or on the stator. The measured torque corresponds to a torque applied to the surface of that object. Consequently, the torque most certainly measures the shear stress in the fluid adjacent to its surface. Stress is communicated through adjacent regions throughout the fluid. At steady state, these forces are in balance, and the shear stress falls off as $1/r^2$ across the gap. However, the stress can fluctuate, and fluctuations in the velocity of fluid layers ensue. This is particularly noticeable at low stresses, where the material response may be nonuniform. Because the transducer can only sense the torque applied at the surface of the object on which it is mounted, the measured torque is different, whether it comes from the stator or from the rotor, when the material response is nonuniform and fluctuations in velocity and stress occur. These differences are observed for the more viscous solution ($R = 2$) at low flow rates. Here, the fluid adjacent to the stator is a slipping block. Slip occurs at the interface (between the stator and the slipping block), and through this interface, the stress is transmitted. The block is continuously elastically deforming (shear rate is approximately zero), storing and releasing energy. Therefore, slip velocity fluctuates, and as a consequence, stress fluctuates. In contrast, a steady shear gradient develops adjacent to the rotor, and more steady stress is transmitted across this interface.

Stress fluctuations in a heterogeneous flow of rodlike particles have been described by taking into account the induced spatial variations of the fluid mesostructure by using a term of the form $\kappa(\dot{\gamma}(y))(d^2/dy^2)\dot{\gamma}(y)$, where y is the velocity gradient direction and $\kappa(\dot{\gamma}(y))$ is a shear curvature viscosity. $\kappa(\dot{\gamma}(y))$ shear thins to zero at the same shear rate where the shear viscosity, $\eta(\dot{\gamma}(y))$, attains its high shear limiting value.[17] The complete expression for the shear stress is a difference of two terms: $\eta(\dot{\gamma}(y))\dot{\gamma}(y) - \kappa(\dot{\gamma}(y))(d^2/dy^2)\dot{\gamma}(y)$. For stationary states, variations of these terms cancel along the fluid, and shear stress becomes uniform. The velocity fluctuations in the band of Figures 2b and 4 might be due to the lack of proper cancellation of these terms. This band is acting as an intermediate region or as an interface, which makes difficult the transduction of stress from the fluid in the linear region to the slipping block that is also slipping on the stator. The slipping block seems to be similar to the equilibrium isotropic phase, leaving the WM almost unaffected by the flow. A thin intermediate region was also found in the WM system CTAB (0.3 M)/KBr (0.3 M)/water[11] under flow. Here, the fluid splits into two homogeneous bands adjacent to the walls of a Couette cell. These bands are separated by a thin zone, where WM orientation with respect to the flow direction varies continuously. As discussed by the authors, it is not clear whether this region is acting as an interface or as a third region.

Shear Stress Fluctuations and Shear Inception Experiments for R = 2. As mentioned, for $\dot{\gamma}_{imp} > 0.45$ s^{-1} (Figure 10), stress oscillations are observed as a function of time when stress is sensed with the stator during the ramping up of a TL under shear strain control. On the other hand, velocity profiles in Figure 6b present velocity fluctuations mainly near the static cylinder when the fluid has not reached a steady state. Therefore, stress oscillations in TL where there was not enough time to reach a steady state and velocity fluctuations should be related. For the same system studied here, but with half of the surfactant concentration, other authors showed that, in the stress plateau, the fluid forms one single band where velocity is fluctuating.[32] This band becomes alternatively turbid and clear as time
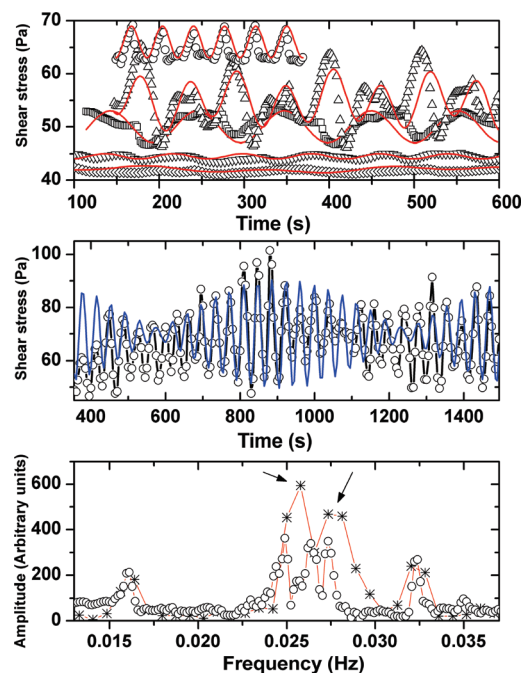

Figure 11. Stress oscillations vs time when shear stress oscillations become periodic at constant imposed shear rate ($R = 2$). (a) Examples of oscillations at different shear rates ($\bigcirc$ 6.0 s^{-1}, $\triangle$ 2.0 s^{-1}, $\square$ 1.0 s^{-1}, $*$ 0.7 s^{-1}, ∇ 0.4 s^{-1}). The lines are fitting obtained by using the most important frequencies after a Fourier analysis. (b) Shear stress oscillations at $\dot{\gamma}_{imp} = 3.5$ s^{-1} ($\bigcirc$) and fitting (—) obtained by using the most important frequencies marked with arrows in the Fourier transform of the stress oscillation shown in panel c. (c) Fourier transforms of two different experiments at $\dot{\gamma}_{imp} = 3.5$ s^{-1}. The most important frequencies are approximately reproducible.

elapses.[31] Unfortunately, their efforts to correlate both, turbidity and velocity close to the moving wall as a function of time, with stress oscillations have not been conclusive.[31,32]

The behavior of stress oscillations can be more clearly observed in shear inception experiments. As mentioned, when shear rate is imposed and stress is sensed with the static cylinder (Ares rheometer), the shear stress average measured after a long time of shearing follows closely the up-shear TL curves (Figure 10, open squares). Shear stress transient response is an increasing function of time when $\dot{\gamma}_{imp} < 0.1$ s^{-1} (not shown) following the short-time transient relaxation curve typical of Maxwell viscoelastic fluids.[44] However, when $\dot{\gamma}_{imp} \geq 0.1$ s^{-1}, the stress response in shear inception experiments oscillates. Typically, two or three high-amplitude stress oscillations take place during the first 150 s, reaching even negative stress values[44] because of the elastic character of the sample (not shown). After this period of time, stress oscillations become periodic around a mean value, as shown in Figure 11. Some stress oscillations were followed for more than one hour, and during this period of time, the amplitude of the oscillations did not decline. By using Fourier analysis, we can distinguish several dominant frequencies in the stress oscillations. The frequency with the highest amplitude coincides always with the Couette cylinder angular frequency. Figure 11a,b shows typical stress oscillations for different $\dot{\gamma}_{imp}$ when oscillations have become periodic. Each curve was fitted with one or two sinusoidal functions depending on the relative importance of the different angular frequencies found in the Fourier spectrum. In Figure 11c, we present a typical example of the Fourier transform for shear stress oscillations in two different experiments at $\dot{\gamma}_{imp} = 3.5$ s^{-1}. In particular, for $\dot{\gamma}_{imp} = 0.4$ s^{-1}, we used just one sinusoidal function to fit the stress oscillation (Figure 11a). For $\dot{\gamma}_{imp} = 2$

s^{-1} (Figure 11a) and for $\dot{\gamma}_{imp}$= 3.5 s^{-1} (Figure 11b), two sinusoidal functions were used to fit the experimental oscillation curve. Several researchers using a Couette cell[31,32] have found similar frequency spectra for stress oscillations for the same system of interest here. We confirm their observations about the shape of stress oscillations. Signals grow steadily as a function of time, and after a maximum, they drop down abruptly. Nevertheless, in contrast with those researchers, we have found stress oscillations at shear rates as low as $\dot{\gamma}_{imp} \approx 0.1$ s^{-1} and along the entire stress plateau. For these authors,[31,32] the dominant frequencies also increase with $\dot{\gamma}_{imp}$, but they did not report that the highest-amplitude frequency coincides with the Couette cylinder angular frequency. This oscillation behavior according to the velocity profiles presented in this work must be related to slipping. A more refined study has to be done; it is underway.

Conclusion

We compared the rheological behavior of two Maxwellian WM solutions at $R = 2$ and at $R = 4$ in the semidilute regime close to the concentrated regime under Couette flow. We found that the fluid in an apparent stationary flow at $R = 2$ becomes heterogeneous, even at very low $\dot{\gamma}_{imp}$, but velocity profiles do not necessarily correspond with a gradient shear banding. When $\dot{\gamma}_{imp}$ is in the ascending part of the flow curve, a continuous alignment of WMs is taking place. At these low $\dot{\gamma}_{imp}$, a long time after flow inception, the fluid presents one region close to the moving cylinder where the local mean velocity depends linearly on the gap position and another region close to the static cylinder forming a slipping block. On increasing $\dot{\gamma}_{imp}$, this block can flow, and velocity profiles define two or three regions, as well as velocity fluctuations at large sectors not always in the same position. When $\dot{\gamma}_{imp}$ corresponds to the values of the plateau, $\dot{\gamma}_{imp} > 0.45$ s^{-1}, velocity profiles are consistent with gradient shear banding, where the fluid approximately follows the lever rule. On the contrary, for $R = 4$, the flow never becomes heterogeneous even at high shear rates. Depending on the kind of instrument used to make rheometric measurements in Couette flow, we observed important qualitative differences between flow curves at $R = 2$ but not at $R = 4$. Velocity profiles could explain these differences between flow curves for both R values and reveal that it is important to take care of the way in which shear stress is measured when the fluid splits into regions or slip is present.

One important feature in this system is that the picture of two stable shear bands separated by a thin steady interface is not always valid. Inhomogeneous flow could be observed, although it cannot be classified as shear banding. In addition, conditions can be found where, as shear rate is increased and before shear banding appears, instead of a thin interface, a fluctuating intermediate band can be observed.

Finally, this work shows that Doppler technique is useful to determine velocity profiles in wormicellar solutions, although it is quite sensible to velocity fluctuations.

References and Notes

(1) Berret, J. F. Rheology of Wormlike Micelles: Equilibrium Properties and Shear Banding Transitions. In *Molecular Gels. Materials with Self-Assembled Fibrillar Networks*; Weiss, R. G., Terech, P. , Eds; Springer: The Netherlands, 2006; p 663.

(2) Cates, M. E. *Macromolecules.* **1987**, *20*, 2289.

(3) Walker, L. M. *Curr. Opin. Colloid Interface Sci.* **2001**, *6*, 451.

(4) Cappelaerre, E.; Berret, J.-F.; Decruppe, J. P.; Cressely, R.; Lindner, P. *Phys. Rev. E* **1997**, *56*, 1869.

(5) Berret, J.-F.; Porte, G.; Decruppe, J.-P. *Phys. Rev. E* **1997**, *55*, 1668.

(6) Herle, V.; Kohlbrecher, J.; Pfister, B.; Fischer, P.; Windhab, E. *J. Phys. Rev. Lett.* **2007**, *99*, 158302.

(7) Olmsted, P. D.; Lu, C. Y. D. *Phys. Rev. E* **1999**, *60*, 4397.

(8) Fielding, S. M.; Olmsted, P. D. *Eur. Phys. J. E* **2003**, *11*, 65.

(9) Lerouge, S.; Decruppe, J. P.; Berret, J. F. *Langmuir.* **2000**, *16*, 6464.

(10) Wang, S.-Q.; Gelbart, W. M.; Ben-Shaul, A. *J. Phys. Chem.* **1990**, *94*, 2219.

(11) Lerouge, S.; Decruppe, J. P.; Olmsted, P. *Langmuir* **2004**, *20*, 11355.

(12) Delgado, J.; Castillo, R. *J. Colloid Interface Sci.* **2007**, *312*, 481.

(13) Olmsted, P. D. *Eurphys. Lett.* **1999**, *48*, 339.

(14) Lerouge, S.; Argentina, M.; Decruppe, J. P. *Phys. Rev. Lett.* **2006**, *96*, 88301.

(15) Wilson, H. J.; Fielding, S. M. *J. Non-Newtonian Fluid Mech.* **2006**, *138*, 181.

(16) Fielding, S. M. *Phys. Rev. Lett.* **2005**, *95*, 134501.

(17) Dhont, J. K. G. *Phys. Rev. E.* **1999**, *60*, 4534.

(18) Fielding, S. M. *Soft Matter* **2007**, *3*, 1262.

(19) Fielding, S. M.; Olmsted, P. D. *Phys. Rev. Lett.* **2004**, *92*, 84502.

(20) Porte, G.; Berret, J.-F.; Harden, J. L. *J. Phys. II France* **1997**, *7*, 459.

(21) Olmsted, P. D.; Lu, C.-Y. D. *Phys. Rev. E* **1997**, *56*, R 55.

(22) Olmsted, P. D.; Lu, C.-Y. D. *Faraday Discuss.* **1999**, *122*, 183.

(23) Salmon, J. B.; Collin, A.; Manneville, S. *Phys. Rev. Lett.* **2003**, *90*, 228303.

(24) Fischer, E.; Callaghan, P. T. *Europhys. Lett.* **2000**, *50*, 803.

(25) Fischer, E.; Callaghan, P. T. *Phys. Rev. E* **2001**, *64*, 11501.

(26) López-González, M. R.; Colmes, W. M.; Callaghan, P. T.; Photinos, P. J. *Phys. Rev. Lett.* **2004**, *93*, 268302.

(27) Holmes, W. M.; Lopez-Gonzalez, M. R.; Callaghan, P. T. *Europhys Lett.* **2003**, *64*, 274.

(28) Shikata, T.; Hirata, H.; Kotaka, T. *Langmuir* **1987**, *3*, 1081.

(29) Shikata, T.; Hirata, H.; Kotaka, T. *Langmuir* **1988**, *4*, 354.

(30) Humbert, C.; Decruppe, J. P. *Eur. Phys. J. B* **1998**, *6*, 511.

(31) Azzouzi, H.; Decruppe, J. P.; Lerouge, S.; Greffier, O. *Eur. Phys. J. E* **2005**, *17*, 507.

(32) Decruppe, J. P.; Greffier, O.; Manneville, S.; Lerouge, S. *Phys Rev. E* **2006**, *73*, 61509.

(33) Lerouge, S.; Decruppe, J. P.; Humbert, C. *Phys. Rev. Lett.* **1998**, *81*, 5457.

(34) Galvan-Miyosyi, J.; Delgado, J.; Castillo, R. *Eur. Phys. J. E* **2008**, *26*, 369.

(35) Salmon, J. B.; Manneville, S.; Colin, A.; Pouligny, B. *Eur. Phys. J. AP* **2003**, *22*, 143.

(36) Fuller, G. G. *Optical Rheometry of Complex Fluids*, 1st ed.; Oxford University Press, 1995.

(37) Inoue, T.; Inoue, Y.; Watanabe, H. *Langmuir* **2005**, *21*, 1201.

(38) Fuller, G. G.; Mikkelsen, K. J. *J. Rheol.* **1989**, *33*, 761.

(39) Lenstra, T. A. J. Colloids near phase transition lines under shear. Ph.D. Dissertation, University of Utrecht, The Netherlands, 2001.

(40) Wang, S. Q.; Ravindranath, S.; Boukany, P.; Olechnowicz, M.; Quirk, R. P.; Halsa, A.; Mays, J. *Phys. Rev. Lett.* **2006**, *97*, 187801.

(41) Tapadia, P.; Ravindranath, S.; Wang, S. Q. *Phys. Rev. Lett.* **2006**, *96*, 196001.

(42) de Gennes, P. G. *Eur. Phys. J. E* **2007**, *23*, 3.

(43) Brochard, F.; de Gennes, P. G. *Langmuir* **1992**, *8*, 3033.

(44) Berret, J.-F. *Langmuir* **1997**, *13*, 2227.